Strengthening mechanisms and strain hardening behavior of 316L stainless steel manufactured by laser-based powder bed fusion

Aliakbar Taghipour [a], Yousef Mazaheri [b,*], Jascha McDavid [c], Shahram Sheikhi [c], Moritz Braun [a], Junjun Shen [d], Benjamin Klusemann [d,e], Sören Ehlers [a,f]

[a] Institute for Ship Structural Design and Analysis, Hamburg University of Technology, Am Schwarzenberg-Campus 4 (C), 21073 Hamburg, Germany

[b] Department of Materials Science and Engineering, School of Engineering, Shiraz University, Shiraz, 71946-84334, Iran

[c] Institute of Materials Science and Joining Technology, Hamburg University of Applied Science, Berliner Tor 5, 20099 Hamburg, Germany

[d] Solid State Materials Processing, Institute of Materials Mechanics, Helmholtz-Zentrum Hereon, Max-Planck Straße 1, 21502 Geesthacht, Germany

[e] Institute for Product and Process Innovation, Leuphana University of Lüneberg, Universitätsallee 1, 21335 Lüneburg, Germany

[f] Institute of Maritime Energy Systems, German Aerospace Center (DLR), 21502 Geesthacht, Germany

*Corresponding author

E–mail: yousef.mazaheri@shirazu.ac.ir

Abstract

The microstructure-properties relations and strengthening mechanisms of additively manufactured 316L stainless steel is comprehensively investigated in this work. The orientation dependency and the strain hardening are studied by tensile testing of as-built specimens fabricated by laser-based powder bed fusion (LPBF) in different directions. The results are compared with those obtained for wrought material. The microstructure of the wrought and the LPBF materials are also comprehensively investigated. Equiaxed grains with random orientation and relatively uniform size

This article has been accepted for publication and undergone full peer review but has not been through the copyediting, typesetting, pagination and proofreading process, which may lead to differences between this version and the Version of Record. Please cite this article as doi: 10.1002/adem.202201230.

(~30 µm) are observed in the wrought material, where the LPBF samples showed columnar grains inside as well as fine equiaxed grains in the bottom of the molten pool. A bimodal grain size distribution, higher values of geometrically necessary dislocations density (~25-32%) and lower fractions of high-angle grain boundaries (~24-28%) is observed in LPBF 316L. A significant yield strength and considerable ultimate strength improvement without remarkable elongation decrease is obtained for the LPBF tensile specimens, resulting in a high strength-elongation balance (up to 26122 MPa%). Two-stage strain hardening is depicted in both wrought and LPBF samples. However, the LPBF samples illustrated lower strain hardening exponents in comparison with the wrought ones. The plastic region of true stress-strain curves is successfully predicted with two-stage Hollomon analysis results.

Keywords: 316L stainless steel; Additive manufacturing; Strain hardening; Mechanical properties; Orientation dependency

1. Introduction

Three-dimensional (3D) printing or additive manufacturing (AM) is a rapidly advancing technology that produces parts directly from digital 3D models by joining materials layer-on-layer. AM is particularly suitable for lightweight structures with complex geometries, low-volume components and custom-made products [1,2]. Selective laser melting (SLM), also known as direct metal laser melting (DMLM) or laser-based powder bed fusion (LPBF), is the most widely used AM technology for manufacturing of metallic parts [3]. Whithin this process, a thin powder layer is applied onto a building platform, where powder particles are selectively fused by a laser beam (scanning). The whole part is built by the repetition of this process. LPBF enables complex lightweight structures - avoiding the application of extensive additional operations such as machining [1-3].

The austenitic chromium-nickel 316 stainless steel contains a deliberate amount of molybdenum, which highly increases corrosion resistance and considerably improves its pitting resistance to chloride ion solutions [4]. AISI 316L, also known as 1.4404 stainless steel, is the very-low carbon version of 316 stainless steel with minimal harmful carbide precipitation during welding. Due to the combination of good mechanical properties at high and very low temperatures, excellent corrosion resistance as well as high machinability, formability and weldability, AISI 316L is used as general-purpose material [4]. It is widely used in marine applications, hydrogen atmospheres or hydrogen piping/cooling applications, low-temperature structural applications, etc. [4]. It has been widely applied in many laser-based AM processing investigations due to its excellent weldability and wide range of applications [4-7]. Additively manufactured 316L is often applied in high value-added scenarios such as medical and dental applications, heat exchangers and lightweight structures [8].

Effects of processing parameters [9-12], microstructural features [13-15], and mechanical properties [16-19] of additively manufactured 316L stainless steel have been well investigated. Its mechanical behavior is also numerically simulated using micromechanical crystal plasticity computations [20-22]. However, some scientific issues have not been well investigated yet. The strain hardening behavior and strength-elongation balance are going to be further investigated in this research. The strain hardening behavior is a particularly crucial factor that describe the deformation behavior and energy absorption of any material. The strain hardening characteristics have been described by a variety of empirical stress-strain correlations, e.g. the models by Hollomon [23], Ludwik [24] and Swift [25]. The Hollomon equation [23], as the most commonly used model, describes the uniaxial strain hardening behavior as

$$\sigma = k\varepsilon^n \tag{1}$$

Consequently [23]:

$$n = \frac{d(\ln\sigma)}{d(\ln\varepsilon)} \tag{2}$$

where n is the strain hardening exponent, k is the strength coefficient and σ and ε are the true uniaxial stress and strain, respectively. The slope and intercept of ln σ versus ln ε plots yield the n and k parameters, respectively.

The strain hardening behavior of wrought 316L stainless steel has been comprehensively investigated in the previous works. Kashyap and Tangri [26] used Hollomon relation and found three distinct regions in terms of the strain hardening behavior of 316L stainless steel and reported the corresponding n and k values. It was observed that larger grains result in lower work hardening rates. In contrast, Ulvan et al. [27] reported that the value of strain hardening parameters (n and k) increases with larger grain size. Sohrabi et al. [28] also reported higher strain hardening exponent (0.72) for the coarse-grained stainless steel (with the average grain size of 76.7 μm) in comparison with the fine-grained sample (with the average grain size of 0.4 μm and the strain hardening exponent of 0.32). Singh [29] reported that at low (room temperature) and intermediate (400 ºC) temperatures, logarithmic stress-strain curves of 316L stainless steel can be fitted by two different lines corresponding to low and high strain regimes. Only at high temperature (800 ºC), the stress-strain response could be described by a single set of parameters [29].

Khodabakhshi et al. [30] compared a laser additively manufactured 316L stainless steel with commercial wrought material and observed one-stage strain hardening, where the reported strain hardening exponent was higher for the AM material. In contrast, Li et al. [31] found that a single power-law fit cannot describe AM samples. A few researchers [32-35] also pointed out the effect of the sample orientation on the strain hardening behavior. To the best knowledge of the authors, a thorough investigation of this property in the LPBF 316L stainless steel including a comparison with wrought material and its possible orientation dependency was not done in the previous studies. Hence, the strain hardening behavior of the wrought and LPBF 316L stainless steel and their orientation dependency were investigated in detail in this study. In addition, the fabricated LPBF 316L stainless steel was compared with those reported in the literature in terms of the strength-elongation balance, which is a good indicator of energy absorption.

2. Experimental procedures

Gas-atomized powder of 316L stainless steel was used for the AM process. Table 1 gives the chemical composition of the powder, which agrees to the reported values for AISI 316L [4].

Table 1. Chemical compositions of the used 316L stainless steel powder

Element	C	Mo	Ni	Mn	Cr	Si	Fe
Composition (wt. %)	0.006	2.5	12.5	1.5	16.6	0.7	Balance

The samples were fabricated in an AM250 LPBF machine from Renishaw. The process parameters, chosen according to the manufacturer recommendation [36,37], are summarized in Table 2.

Table 2. Process parameters used for the fabrication of LPBF 316L stainless steel specimens

Parameter	Value
Laser power (W)	100–180
Layer thickness (μm)	40
Powder density (g/cm^3)	4.29
Width of molten pool (μm)	115
Exposure time (μs)	80
Scan line spacing (μm)	65

The size and distribution of volumetric defects were investigated using a Carl Zeiss Xradia Versa 520 X-ray micro-computed tomography (XCT) scanning with a voxel size of about 4.1 μm. Cylindrical LPBF 316L samples in vertical direction which had 4 mm diameter and 8 mm height were prepared to study the internal defects by XCT scanning.

As wrought samples, rolled and annealed 316L stainless steel sheets with a standard AISI 316L chemical composition were used for comparison. Cuboid wrought and LPBF 316L samples were prepared to study their microstructures. The microstructures were examined by an Union Versamet-

2 optical microscope (OM). Electron backscatter diffraction (EBSD) data was collected via an FEI Quanta 650 FEG scanning electron microscope, including high velocity EBSD system. EBSD mapping was performed at 25 kV accelerating voltage and 0.5 µm step size. Each scanning area was set to 699 × 547.8 µm^2. The microstructural characteristics were assessed by EBSD inverse pole figure (IPF) maps superimposed with image quality (IQ), grain boundary misorientation (GB) maps and geometrically necessary dislocations (GNDs) distribution maps.

The tensile specimens were designed based on the DIN 50125 standard [38], see Fig. 1. All samples were provided with an allowance of 1 mm over the entire gauge length which was removed by electron discharge machining (EDM) before tensile testing. This post-processing treatment was intended to prevent any influence of the high surface roughness of LPBF components on the tensile test results.

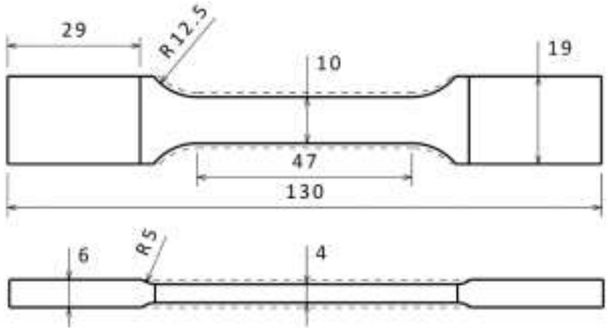

Fig. 1. Geometry of LPBF 316L tensile specimens (dashed lines: initial geometry before EDM, dimensions: mm).

As illustrated in Fig. 2(a), the scanning pattern rotates the laser paths by 67° between successive layers, as explained in [39-41]. It has been shown that this tilt angle results in low anisotropy, defects and residual stresses [42,43]. As illustrated in Fig. 2(b)-(d), some of the uniaxial tensile specimens are produced in horizontal orientation (h) or parallel to building platform plane and some are produced in vertical orientation (v) or building direction. There are two groups of horizontal samples, those that are positioned flat 'hf' and those that are lying on its side 'hs'. For each configuration, nine samples were fabricated, three samples each in 0°, 45° and 90° orientation with respect to the x axis of the building platform. Six tensile samples were also prepared from the rolled plates, three in the rolling direction 'rd' and three in the transversal direction 'td'. The rolled plates are considered to be layed in the xy plane while x and y represent the ‘rd’ and ‘td’, respectively. The tensile tests were conducted according to DIN EN ISO 6892-1 [44] on a Zwick/Roell Z250 machine with crosshead speed of 1 mm/min.

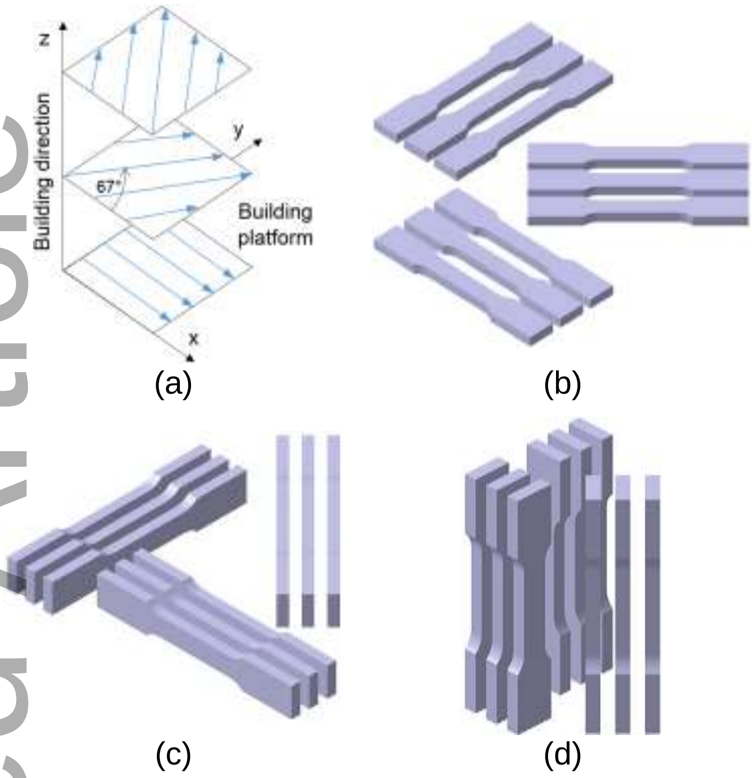

Fig. 2. Scanning strategy (a) and schematic presentation of LPBF 316L specimens' orientation: (b) hf (horizontal, flat), (c) hs (horizontal, lying on it’s side) and (d) v (vertical).

3. Results and discussion

3.1. Defects and microstructure

A random distribution of manufacturing defects throughout the material is observed in all tested LPBF specimens. Fig. 3 shows the typical defects size and distribution obtained over the length of the as-built cylindrical specimens. In Fig. 3(a), all defects are projected on the building platform plane. In addition, the pore volume distribution is shown in Fig. 3(b). The majority of defects are rather small as expected. The defect density is often higher in the proximity of the external surface where large defects are concentrated and it decreases towards the center of the specimen. The thickness of the external layer containing defects is approximately 250 µm, and the volume of the defects is smaller than 4×10^{-4} mm^3. Consequently, removing a 1 mm layer from the exterior of tensile LPBF specimens (see section 2) prevents not only any influence of the high surface roughness but also any influence of the near to surface accumulated defects on the tensile test results.

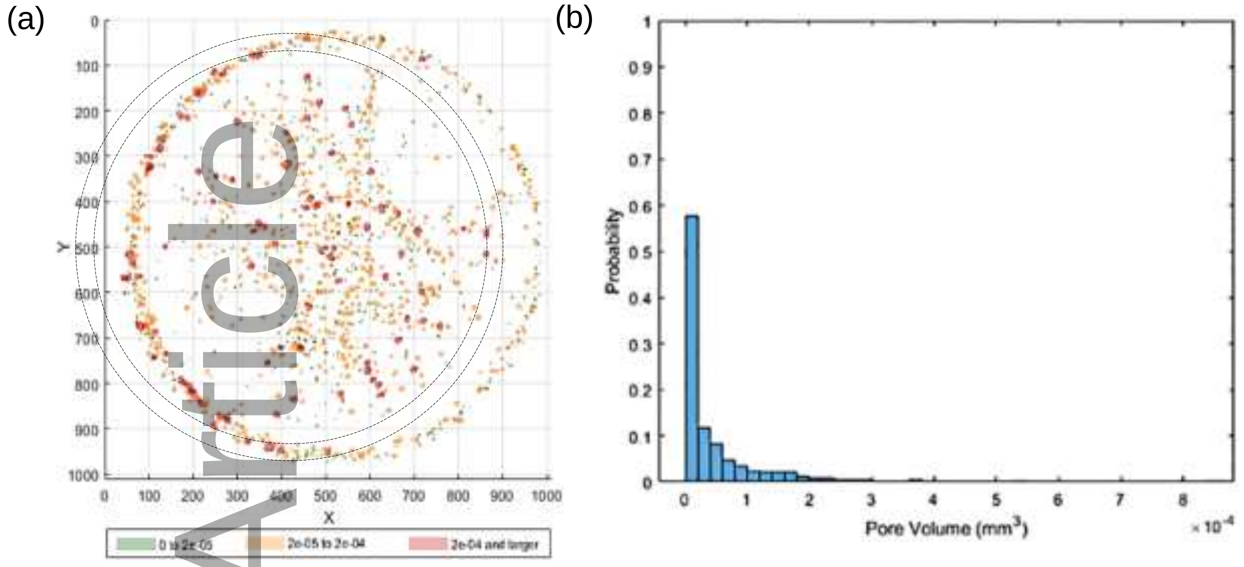

Fig. 3. Typical XCT scan results of an LPBF 316L specimen: (a) projection of all identified defects on the plane normal to building direction and (b) relative frequency of pore volume.

Micrographs of the wrought and LPBF 316L were captured and compared in Fig. 4. The wrought material has equiaxed grains containing twins that is a typical microstructure for rolled and annealed austenitic sheets, see Fig. 4. On the other hand, individual weld beads or molten pools are visible in the LPBF 316L, see Figs. 5(a) and 5(b). The alloy components segregate during the rapid solidification of the melt. Also, the top surface of the melt pool reacts with the atmosphere of the pressure chamber. Consequently the micrographs along the building direction show a layer-like structure, where the melt pool boundaries become visible. This microstructure is totally different from typical austenitic microstructure, as observed for the examined wrought material. The epitaxial crystal growth results in stem crystals, which grow polyhedrically beyond the so-called layered structure. Therefore, the LPBF 316L contains large elongated grains, which favor anisotropic mechanical properties [45].

As reported in [45,46], LPBF leads to highly non-equilibrium microstructures with tortuous and irregular grain morphologies, a high density of dislocations, cellular structures and chemical segregation. Thus, significantly different mechanical properties are expected in comparison with conventional manufacturing routs, such as wrought and cast [47,48]. The xy plane micrograph shows several parallel scan paths or tracks in a longitudinal section, see Fig. 5(c). The AM material examined was not cut out 100% parallel to the xy plane of the sample. Accordingly, the sectional plane shown is inclined minimally to the xy plane. Consequently, several superimposed layers with the relative 67° angle between the scan paths of the successive layers can be identified in the micrograph.

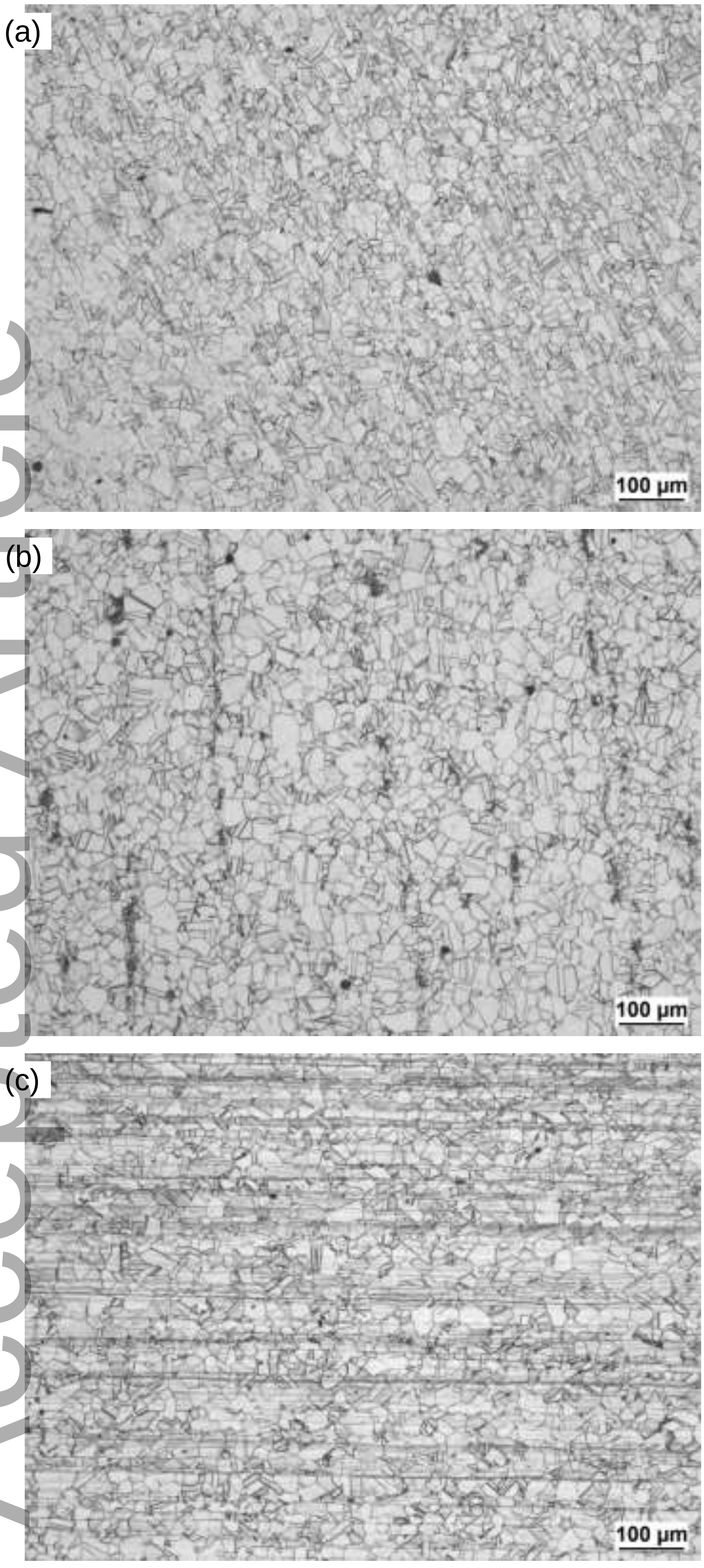

Fig. 4. OM micrographs of wrought 316L stainless steel of different planes: (a) yz, (b) zx and (c) xy.

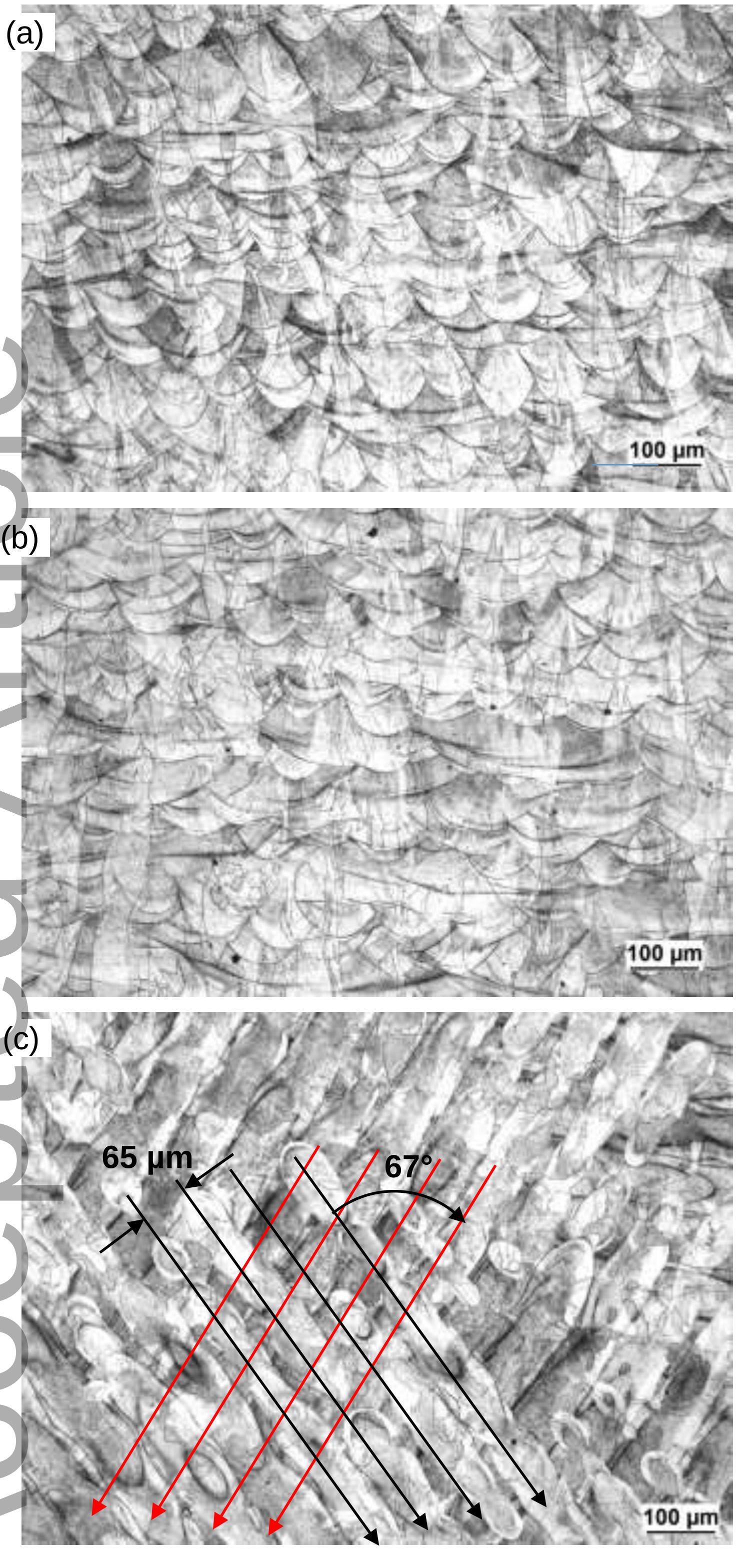

Fig. 5. OM micrographs of LPBF 316L stainless steel of different planes:(a) yz, (b) zx and (c) xy.

The grain size distribution and morphology of the wrought and LPBF 316L samples are characterized by EBSD, see Figs. 6-9. As shown in Fig. 6, wrought 316L is composed of equiaxed grains and twins, corresponding to the results obtained from the OM micrographs shown in Fig. 4. The microstructure is characterized by no pronounced texture and relatively uniform grain size of ~30 μm, see Figs. 6(a-c) and 8(a-c). As indicated in the GB maps, the red lines represent low-angle grain boundaries (LAGBs) with a misorientation angle ranging from 2° to 15°, whereas the black lines characterize high-angle grain boundaries (HAGBs), i.e. GBs with a misorientation angle higher than 15°. The microstructure of the wrought sample mainly consists of HAGBs with an average misorientation angle of about 44°, see Figs. 6(d-f) and 8(d-f). The fraction of HAGBs is 95±1%. These results are in good agreement with those reported by Kong et al. [49].

Figs. 7(a) and 9(a) show the morphology of austenite grains and corresponding grain size distribution of LPBF 316L on zx plane, respectively, which is parallel to the building direction. Coarse columnar grains with an average grain size of ~200 μm, where the grains have grown epitaxial in the building direction and pass through the deposited layers, can be observed. Additionally, few fine equiaxed grains exist in the overlapping zone of the layers with an average grain size of ~50 μm. It is interesting to note that the growth direction of the austenite columnar grains in this plane changes every 40 μm zigzagly. This equals the thickness of a deposited layer. The morphology and size distribution of austenite grains on the yz plane, which is parallel to the building direction, are shown in Figs. 7(b) and 9(b), respectively. The distribution of coarse columnar grains and fine equiaxed grains is bimodal. Compared with the zx plane, equiaxed grains also appear in the overlapping zone, but the size is smaller (~35 μm). In addition, the columnar grains in the yz plane with an average ~150 μm grain size are smaller than that within the zx plane. The LPBF 316L on xy plane, which is parallel to the building platform, Figs. 7(c) and 9(c), is composed of columnar grains with an average ~100 μm grain size in the interior of the molten pool (the non-overlapping zone) and fine equiaxed grains (~25 μm) in the bottom of the molten pool (the overlapping zone) with a bimodal distribution. Although a lot of columnar austenite grains grow close to the building direction, a small amount grow across the deposited layers. The length of most columnar grains equals nearly the thickness of the deposited layer. With considering fraction values, the average grain size is ~147, 114 and 68 μm on the zx, yz, and xy planes, respectively.

Khodabakhshi et al. [30] also observed that the microstructure of AM 316L stainless steel has a bimodal distribution. They reported that coarse columnar grains having ~13.4 μm width, >500 μm length with an aspect ratio of ∼40 were formed at the interface of each layer. Fine equiaxed structures were also found between layers with a mean grain size of ∼22.6 μm. Kong et al. [49] also observed small grains (~26 μm) mainly formed along the boundary of molten pools and big grains (∼58 μm) generated at the interior of the molten pools.

The fraction of LAGBs in LPBF 316L is higher than that of the wrought alloy. The average misorientation angle is about 40°, see Figs. 7(d-f) and 9(d-f). By considering the total length of grain boundaries, the fraction of HAGBs is 68, 72 and 74% on the zx, yz, and xy planes, respectively.

GNDs distribution maps of the wrought and LPBF 316L stainless steel on different planes are presented in Fig. 10. It is obvious that high fractions of GNDs are accumulated on grain boundaries. The average density of GNDs in the wrought sample is 8.67×10^{13}, 7.71×10^{13} and 8.13×10^{13} m^{-2}, and in LPBF 316L is 11.40×10^{13}, 9.59×10^{13} and 9.98×10^{13} m^{-2} on the zx, yz, and xy plane, repectively. Higher values of GNDs density and lower fractions of HAGBs can be attributed to the formation of cell structures in SLM-processed 316L stainless steel, and result in a substantial contribution to material strength [49].

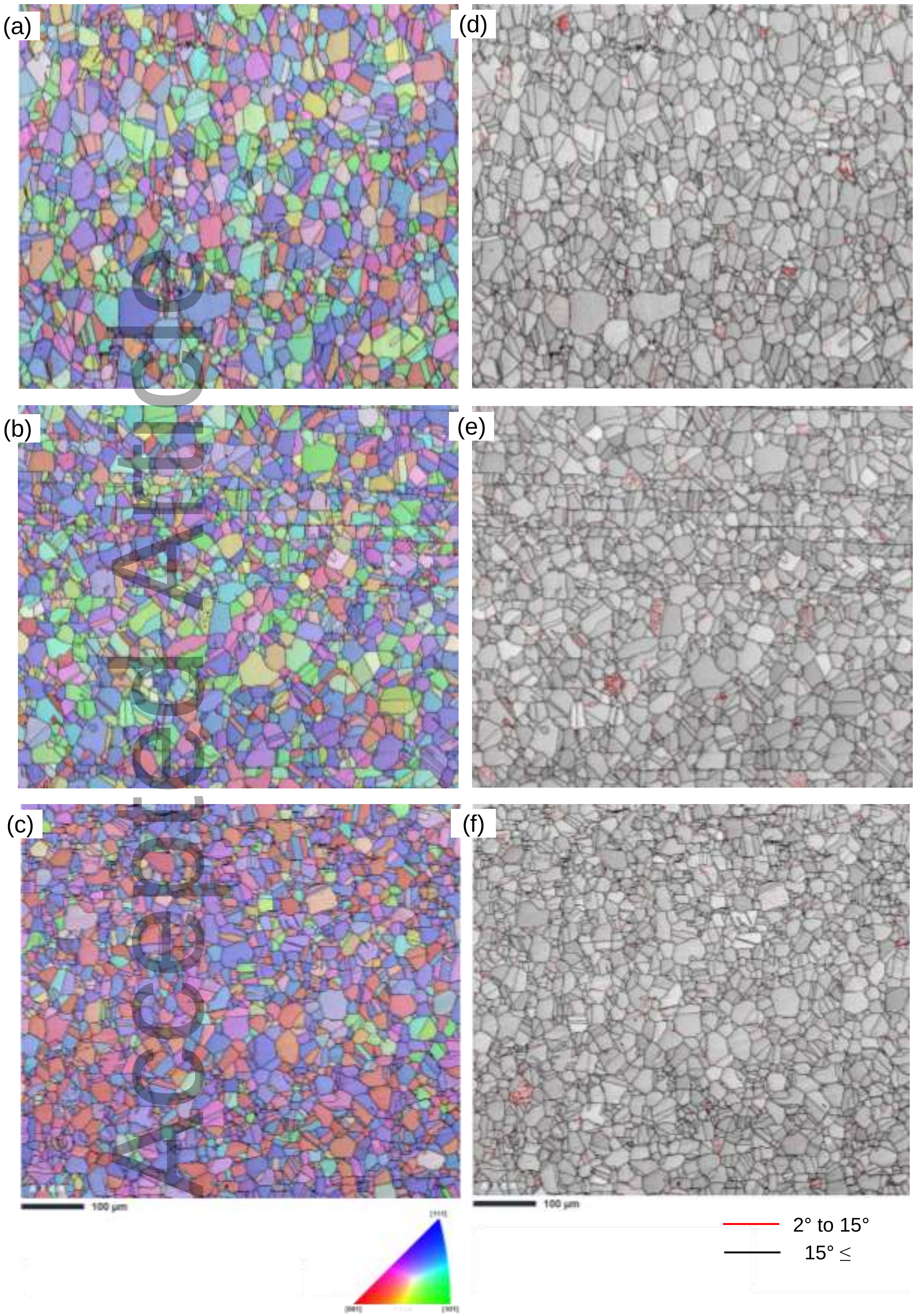

Fig. 6. EBSD IPF (a-c) and GB (d-f) maps of the wrought 316L stainless steel on different planes: (a,d) zx, (b,e) yz, and (c,f) xy.

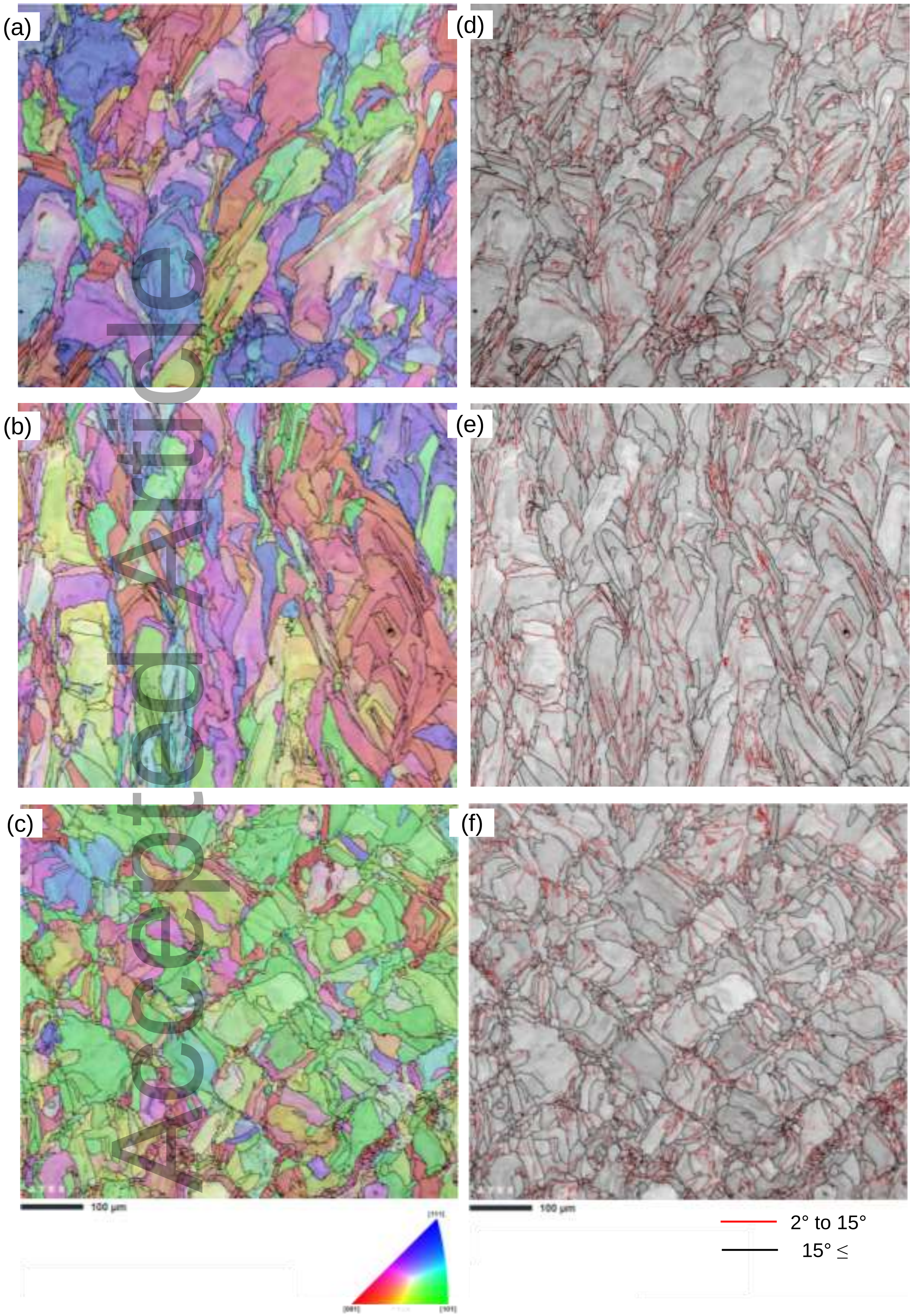

Fig. 7. EBSD IPF (a-c) and GB (d-f) maps of the LPBF 316L stainless steel on different planes: (a,d) zx, (b,e) yz, and (c,f) xy.

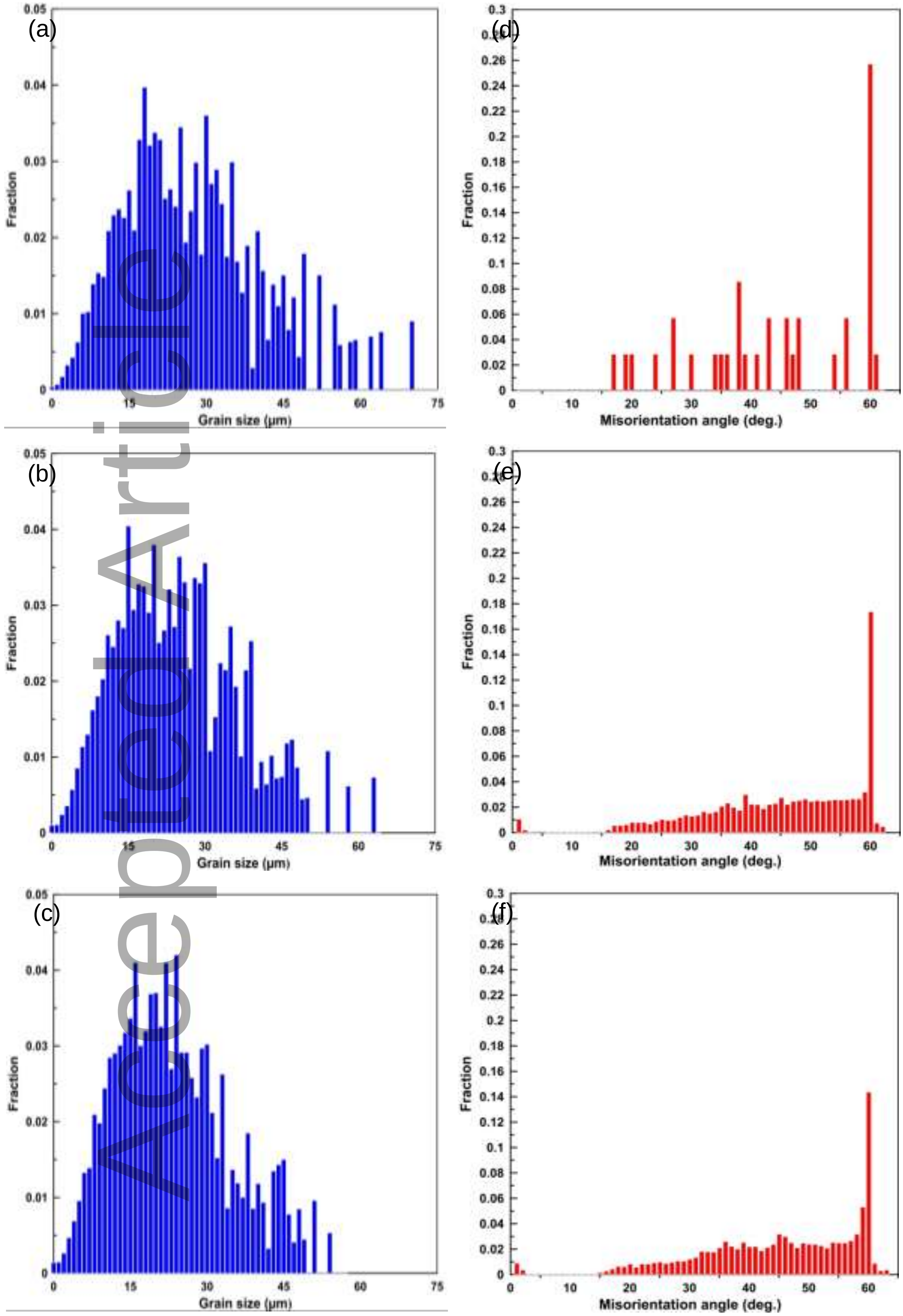

Fig. 8. Grain size (a-c) and Misorientation angle (d-f) distribution of the wrought 316L stainless steel on different planes: (a,d) zx, (b,e) yz, and (c,f) xy.

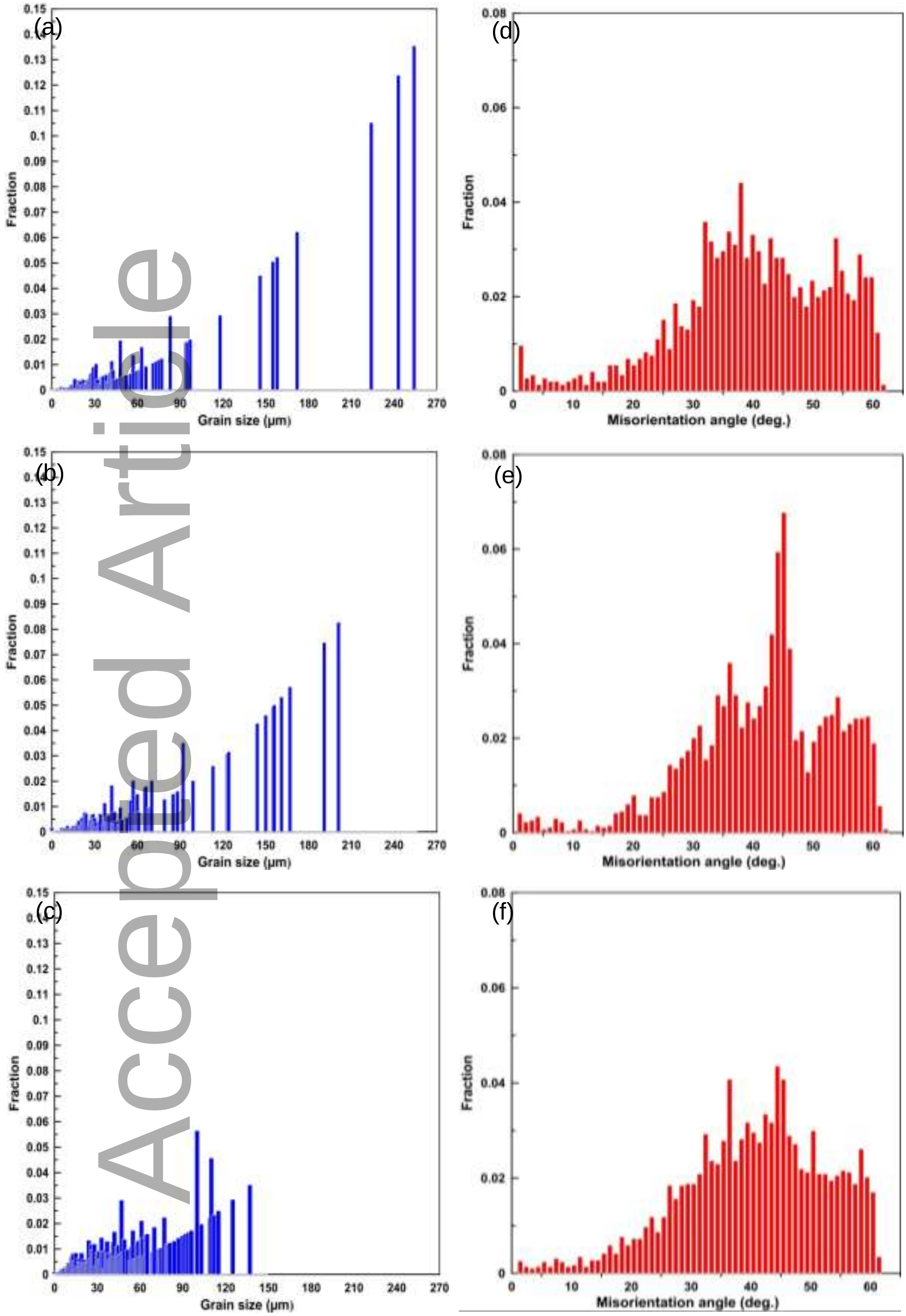

Fig. 9. Grain size (a-c) and misorientation angle (d-f) distribution of the LPBF 316L stainless steel on different planes: (a,d) zx, (b,e) yz, and (c,f) xy.

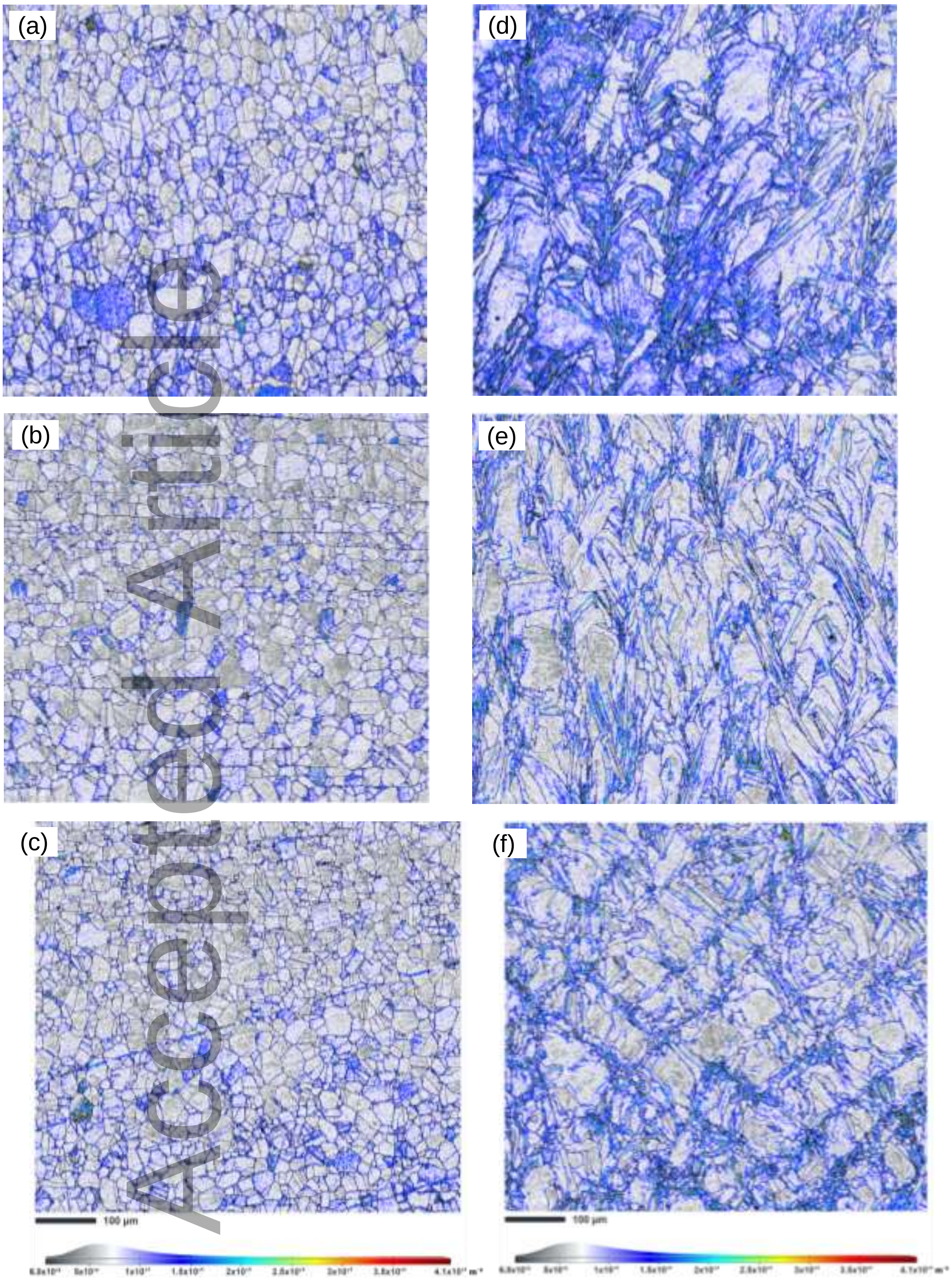

Fig. 10. GNDs distribution maps of the wrought (a-c) and LPBF 316L (d-f) stainless steel on different planes: (a,d) zx, (b,e) yz, and (c,f) xy.

3.2. Tensile properties

Representative engineering and true stress-strain curves of wrought and LPBF 316L with different orientations are presented in Figs. 11 and 12, respectively. The true stress-strain curves are drawn up to uniform elongation identified by the instability criterion. The results of the tensile tests are summarized in Table 3. The wrought material shows a nearly isotropic behavior, see results in and perpendicular to the rolling direction. The isotropy is in particular attributed to the annealing of the rolled plates. In contrast, the LPBF specimens show an anisotropic static mechanical behavior induced by the orientation-dependent microstructural features, see section 3.1. The highest elongation (El), but lowest yield (YS) and ultimate tensile strength (UTS), were observed in building direction, i.e. 'v' specimens. The opposite is true for the 'hf' specimens. The 'hs' specimens are in between the others. Please note that the 'hf' and 'hs' specimens are built parallel to the building platform. The tests show that the tensile properties are not dependent on the different angular printing position of the specimens (0°, 45° and 90°) relative to the building platform, see Fig. 2. This shows that all samples, regardless of their orientation relative to the building platform, experienced the same scanning condition. It can be assumed that a dependency of different angular positions occurs as soon as a relative angular change of the scan paths of successive layers (Fig. 2(a)) does not apply.

The wrought 316L is characterized by a high El but a low YS and low YS/UTS ratio, typical for annealed 316L plates [49-51]. However, LPBF 316L shows a high YS and a high YS/UTS ratio but lower El, see Table 3. The higher strength in several classes of materials produced by SLM has been reported previously [52]. The rapid cooling during LPBF leads to formation of fine-grains in the microstructure. Moreover, the fraction of LAGBs and GNDs in LPBF 316L is high due to its cellular structure, see section 3.1. Consequently, the significantly higher yield strength (>200%) can be related to the difference in the microstructures and Hall–Petch effect, where the conventional grain size has to be replaced with the cell size in the corresponding Hall-Petch relation [31,49,52-54]. A considerable increase in the ultimate strength of 316L up to 130% is obtained for LPBF/M compared to that obtained conventionally. This could be explained by the multi-scale features of the microstructure, in particular the presence of cellular dislocation substructures [55]. The high YS/UTS ratio is also a special feature of LPBF 316L, see Table 3. It is conventionally 0.4-0.5; however, it is 0.8-0.9 in case of LPBF 316L. Typically an increase in this ratio results in a reduction in the elongation at breakage. Probably the hardening induced by LPBF has resulted in this high YS/UTS ratio. The high thermal gradients during the AM process lead to constraints at the grain scale. They create numerous dislocations which are the origin of work hardening [55, 56]. The contributions of different strengthening mechanisms to the yield strength (σ_y) of the LPBF 316L can be considered as follows [57]:

$$\sigma_y = \sigma_0 + \sigma_g + \sigma_d \tag{3}$$

where σ_0, σ_g and σ_d are intrinsic yield strength, grain boundary and dislocations strengthening, respectively. The σ_0 of 316L stainless steel is reported as about 207.4 MPa [26]. The contribution of σ_g can be expressed via the Hall-Petch relation [26]:

$$\sigma_g = kd^{-1/2} \tag{4}$$

where d represents the mean grain size; k is the coefficient of strengthening and is reported as about 300 MPa μm$^{1/2}$ for 316L stainless steel [26]. By introducing the average grain size values of 147, 114 and 68 μm on the zx, yz, and xy planes (see section 3.1) in Eq. (4), the σ_g contributions can be calculated as 24.7, 28.1 and 36.4 MPa, respectively. The dislocation strengthening contribution σ_d is determined by the Taylor equation [57]:

$$\sigma_d = \alpha M \mu b \rho^{1/2} \tag{5}$$

with ρ being the dislocation density. α is an adjustable parameter, taken here as 0.5. M represents the Taylor factor, which is determined as 3.35 [57]. The shear modulus μ of this stainless steel is 78000 MPa. The Burger's vector magnitude b is 0.245 nm [57]. Using Eq. (5) and the average values of ρ as 11.40×10^{13}, 9.59×10^{13} and 9.98×10^{13} m^{-2} on the zx, yz, and xy plane (see section 3.1), the σ_d contributions can be evaluated as 341.8, 313.4 and 319.7 MPa, respectively.

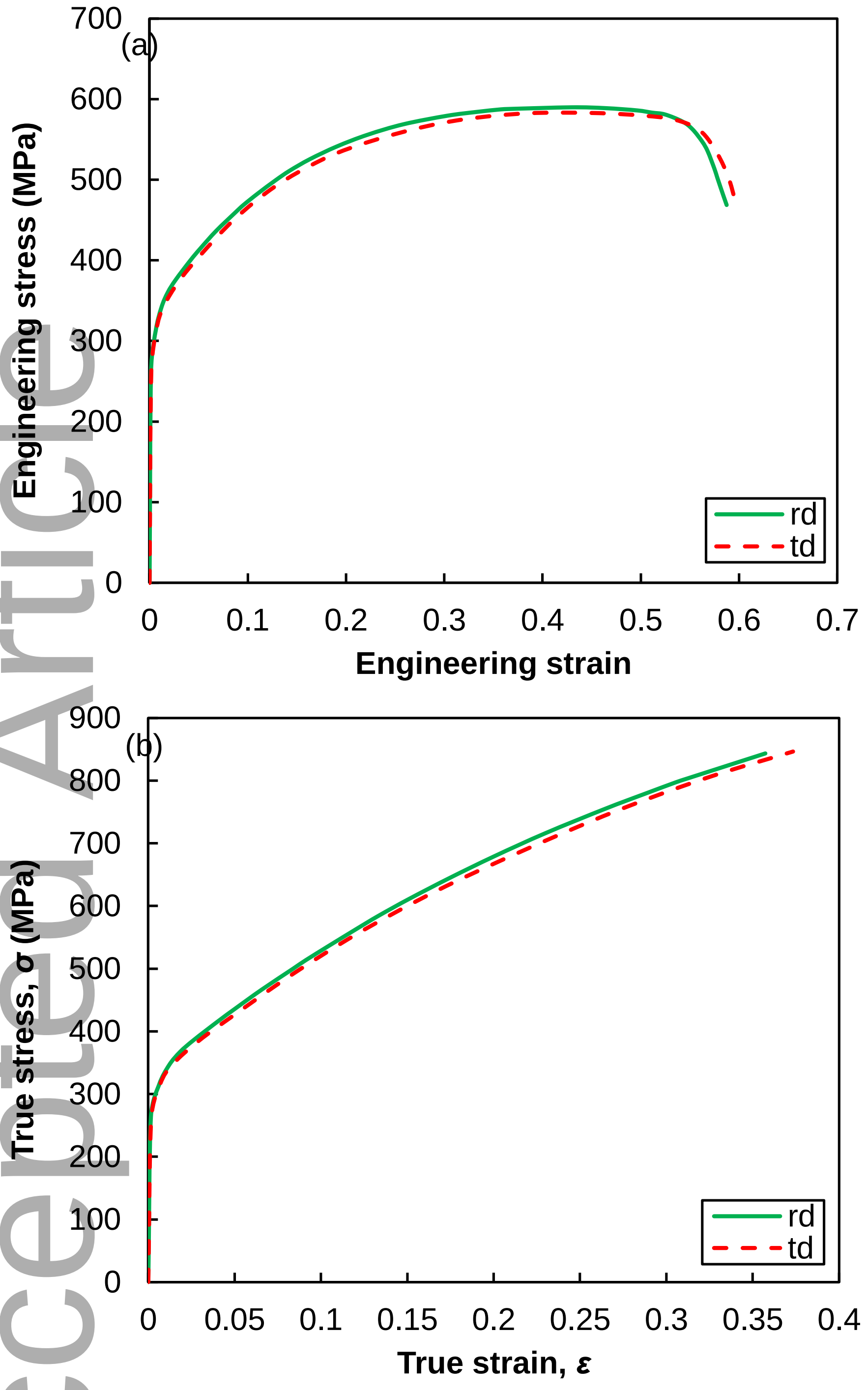

Fig. 11. Representative (a) engineering and (b) true stress-strain curves of the wrought 316L stainless steel specimens with different orientations.

By considering the different strengthening effects, good agreement can be observed between the calculated strength values (549-574 MPa) and the experimental range (510-666 MPa).

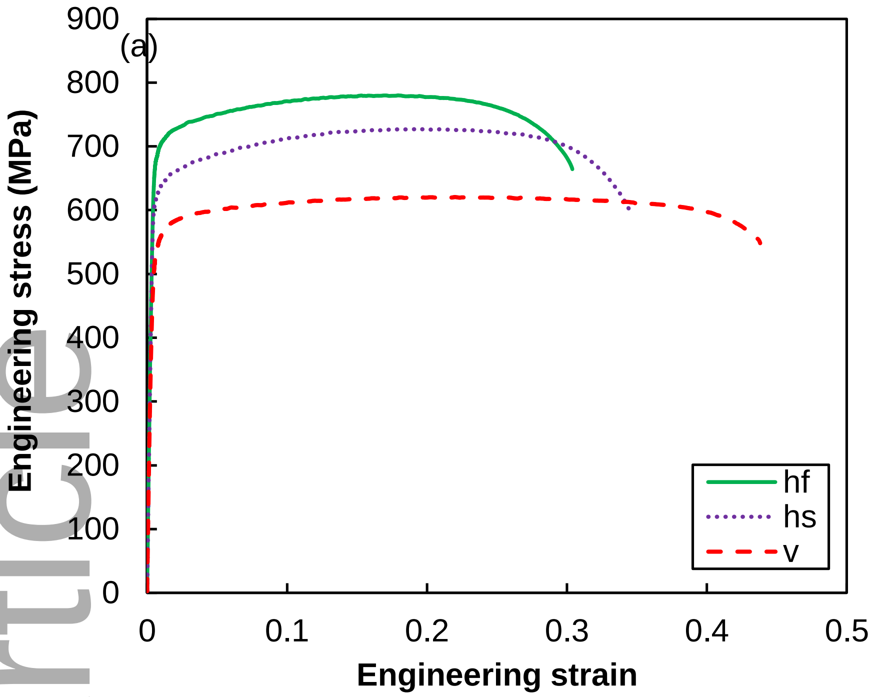

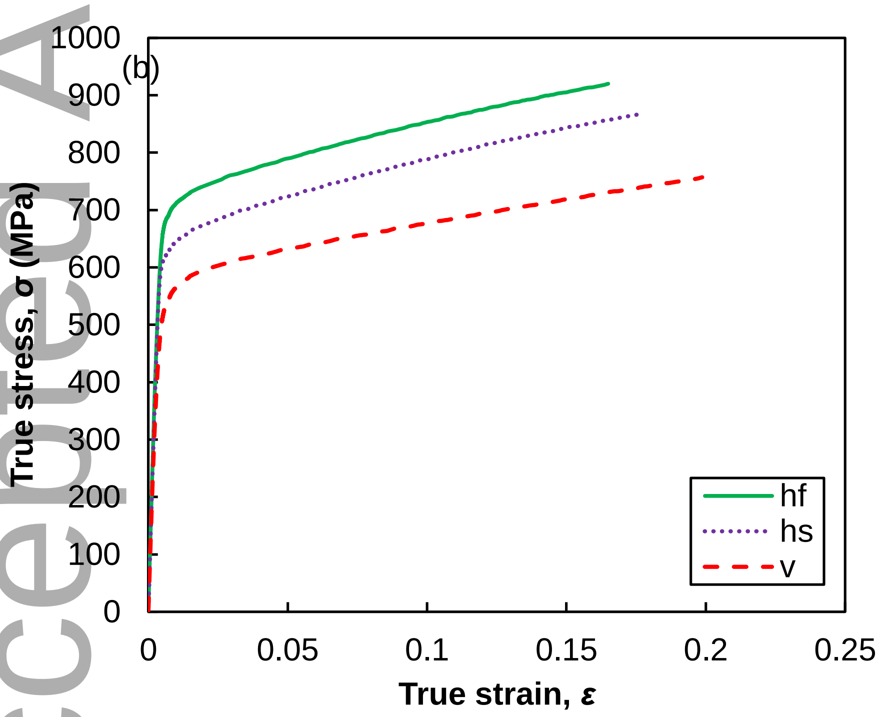

Fig. 12. Representative (a) engineering and (b) true stress-strain curves of the LPBF 316L stainless steel specimens with different orientations.

The obtained mechanical properties in this study are compared to the data from the literature in Table 4. A wide range of property values is observed, which can be attributed to the variety of the processing parameters and different processing machines. The 316L produced in this study has mechanical tensile properties which are comparable to most of the literature results. The strength-elongation balance (UTS×El) is in the upper range and can probably be resulted from the lower defects and porosities [38], which are more numerous in samples produced by SLM.

Table 3. Tensile properties of the different 316L stainless steel specimens

Sample	Orientation	YS (MPa)	UTS (MPa)	YS/UTS	El (%)
Wrought	td	260 ± 20	581 ± 19	0.45	60 ± 2.5
	rd	263 ± 27	589 ± 21	0.45	59.2 ± 2.8
LPBF	v	510 ± 24	619 ± 25	0.82	42.2 ± 3.3
	hs	614 ± 20	727 ± 16	0.84	34.6 ± 2.4
	hf	666 ± 28	778 ± 26	0.86	32.5 ± 4.5

Table 4. Comparison between present work and literature data of the mechanical properties in uniaxial tension of 316L stainless steel obtained by different AM techniques

Reference	YS (MPa)	UTS (MPa)	El (%)	UTS × El (MPa%)
Tolosa et al. [58]	530-560	570-590	42-45	24780-25650
Spierings et al. [59]	640	760	30	22800
Riemer et al. [60]	462	565	54	30510
Wang et al. [16]	590	700	36	25200
Casati et al. [17]	554	685	36	24660
Kuznetsov et al. [61]	567-582	685-708	34-35	23975-24072
Pillot [62]	470-550	540-654	35-50	22890-27000
Liverani et al. [63]	500	570	40	22800
Bahl et al. [54]	480	565	44	24860
Kale et al. [64]	551-571	698-705	16-29	11280-20242
Röttger et al. [65]	209-503	486-644	38-51	24472-24786
Afkhami et al. [32]	475-546	569-656	31-44	20336-25036
Present work	510-666	619-778	32.5-42.2	25285-26122

3.3. Strain hardening behavior

The Hollomon equation [23] is applied to the true stress-strain data and the results are shown in Figs. 13 and 14 and Table 5. All of the samples showed a nonlinear relationship between ln σ and ln ε in a two-stage strain hardening manner with a transition strain between deformation stages (ε_{tr}).

According to the literature, the two hardening stages have been reported where at each stage a certain structural deformation occurred [30-33]. The dislocation density in the vicinity of grain boundaries, is reported to increase upto 4% strain, saturating at ε_{tr} = 5-6% depending on the grain size [66]. Such strains seem to correspond to the end of region I of the curves, Table 5. While the dislocation density grows in the grain interior in the early part of deformation, they attain the same value beyond 5-6% strain as supported by the hardness data [66]. Therefore, region II may represent the homogeneous dislocation distribution interior the grains [26]. Li et al. [31] extracted an *n* value of 0.06-0.07 for most AM samples at 0.01-0.02 strain. This *n* value increases to 0.16-0.19 at 0.10-0.13 strain. This large increase in the strain hardening exponent is related to a shift of deformation mechanisms from dislocation slip to twinning, as observed in *in situ* synchrotron X-ray diffraction experiments [47].

As can be seen in Figs. 13 and 14 and Table 5, the strain hardening exponent of wrought stainless steel is larger than that of the LPBF samples. Other researchers [31,67] pointed out that the heterogeneous and hierarchical microstructures and multiple length scale distributions in AM steels may have a strong influence on the hardening behavior. In addition, the strain hardening behavior is isotropic in wrought stainless steel; however, the *n* and ε_{tr} values are orientation-dependent for LPBF 316L. This is in good agreement with the results of Kumar et al. [33], which observed a texture-dependent strain hardening behavior in AM 316L.

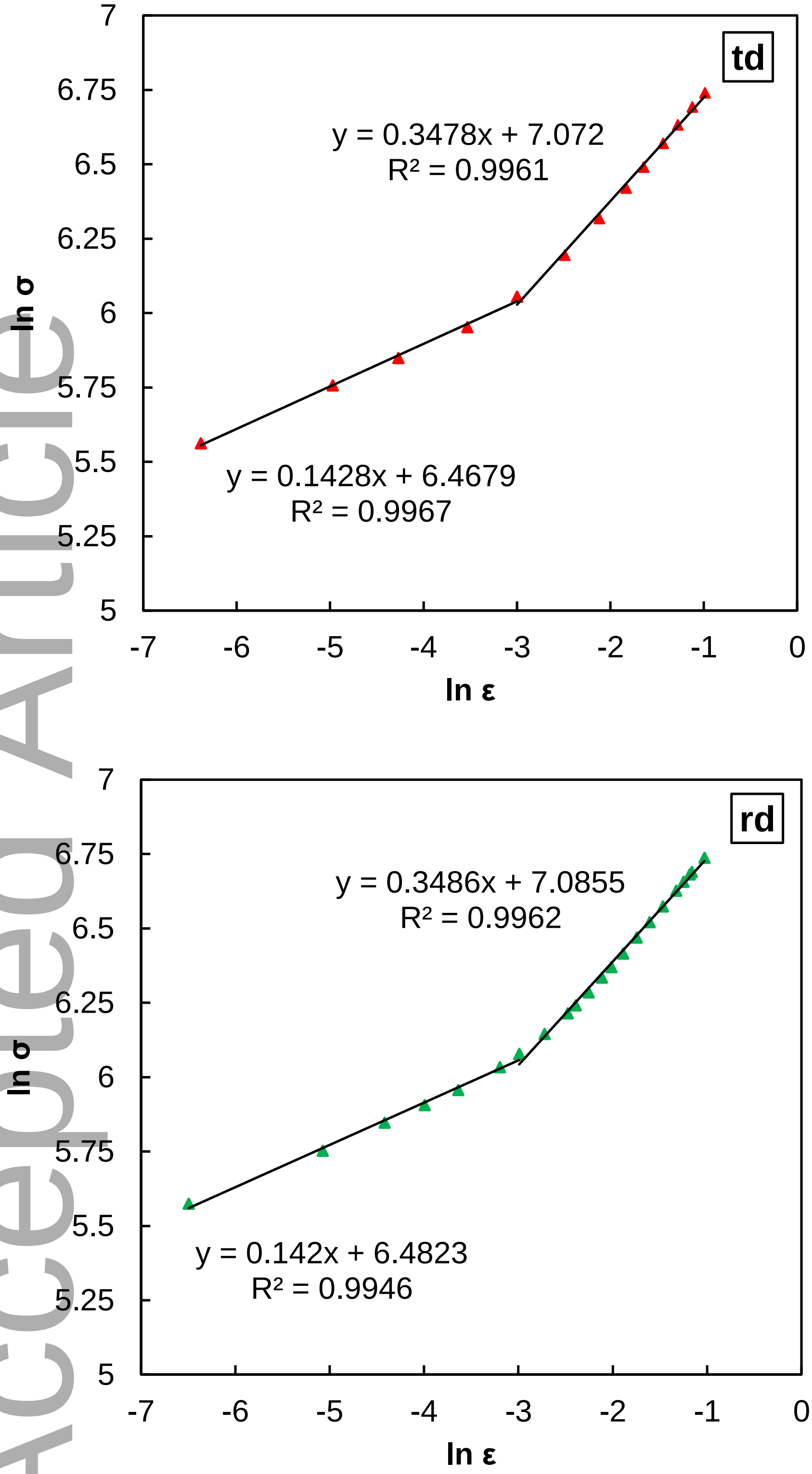

Fig. 13. The ln σ vs. ln ε plots of wrought 316L stainless steel specimens with different orientations.

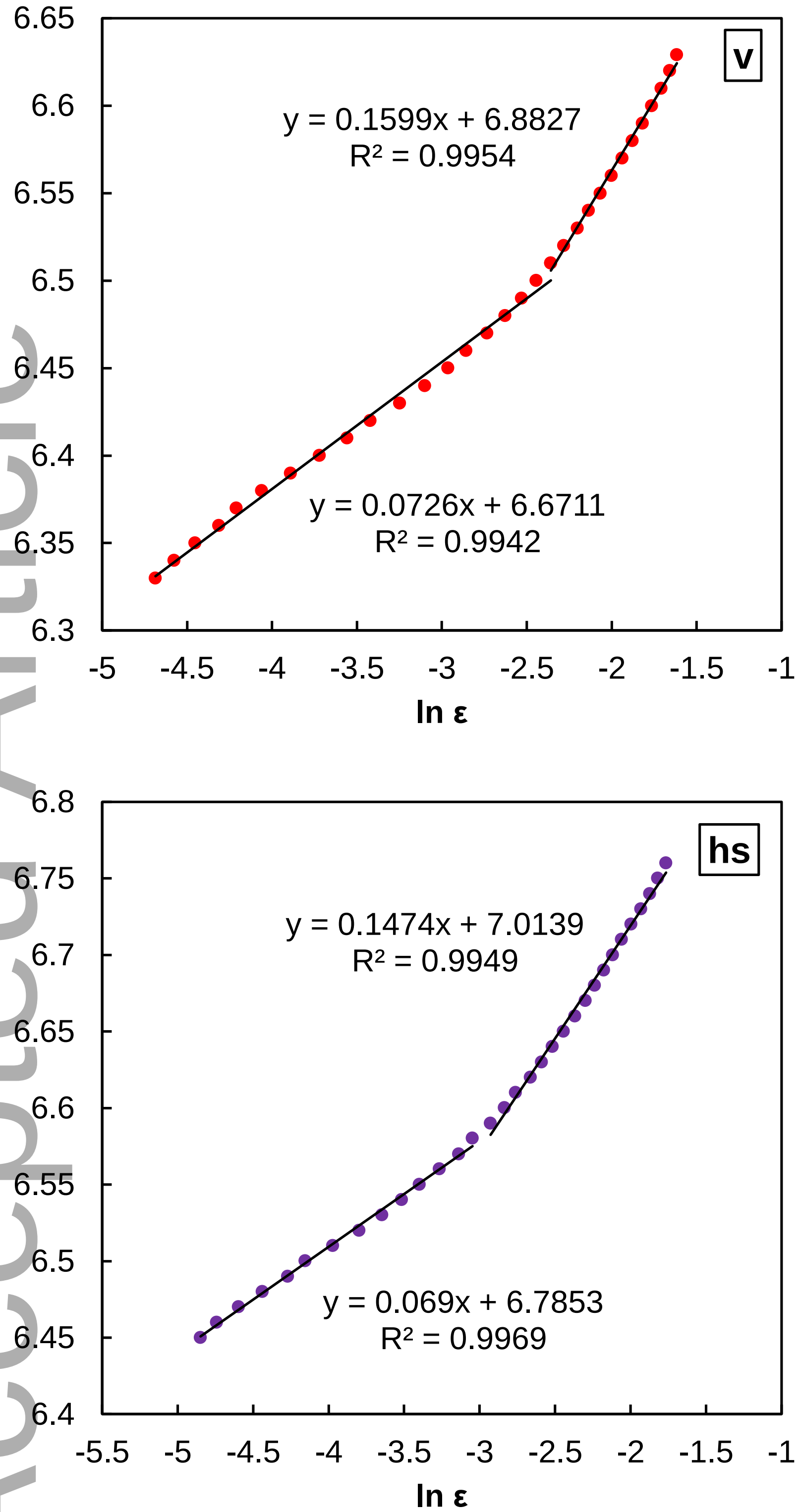
v
y = 0.1599x + 6.8827
R² = 0.9954
y = 0.0726x + 6.6711
R² = 0.9942
ln σ
ln ε
6.65
6.6
6.55
6.5
6.45
6.4
6.35
6.3
-5
-4.5
-4
-3.5
-3
-2.5
-2
-1.5
-1
hs
y = 0.1474x + 7.0139
R² = 0.9949
y = 0.069x + 6.7853
R² = 0.9969
ln σ
ln ε
6.8
6.75
6.7
6.65
6.6
6.55
6.5
6.45
6.4
-5.5
-5
-4.5
-4
-3.5
-3
-2.5
-2
-1.5
-1

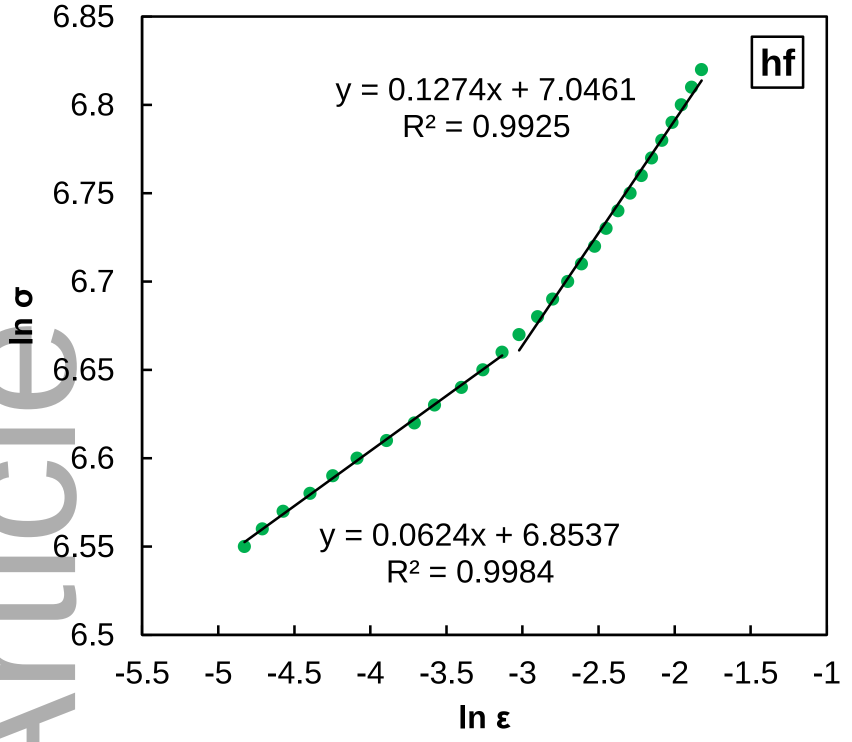

Fig. 14. The ln σ vs. ln ε plots of LPBF 316L stainless steel specimens with different orientations.

Table 5. The parameters of Hollomon equation for wrought and LPBF 316L stainless steel

Sample	Orientation	k_I (MPa)	n_I	k_{II} (MPa)	n_{II}	ε_{tr}
Wrought	td	644.2	0.143	1178.5	0.348	0.050
	rd	653.3	0.142	1195.1	0.349	0.050
LPBF	v	789.2	0.073	975.6	0.160	0.087
	hs	884.5	0.069	1112.1	0.147	0.054
	hf	947.7	0.062	1148.3	0.127	0.044

As shown in Fig. 15, the accuracy of Hollomon analysis is investigated with drawing the experimental and predicted true plastic stress-strain curves together. As illustrated, two-stage Hollomon analysis constants (Table 5) predicts the experimental strain hardening behaviors successfully.

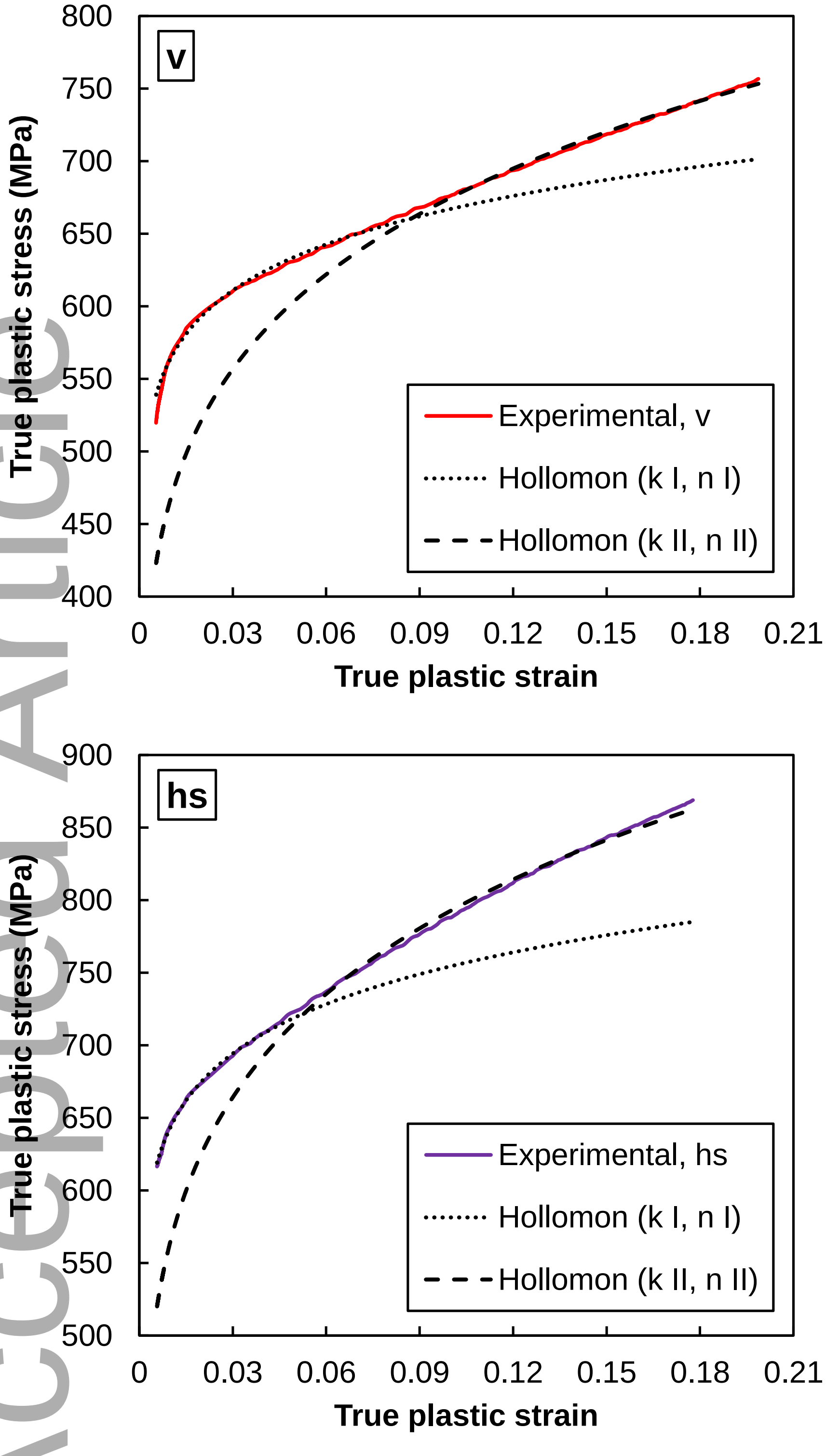
v
Experimental, v
Hollomon (k I, n I)
Hollomon (k II, n II)
True plastic stress (MPa)
True plastic strain
hs
Experimental, hs
Hollomon (k I, n I)
Hollomon (k II, n II)
True plastic stress (MPa)
True plastic strain

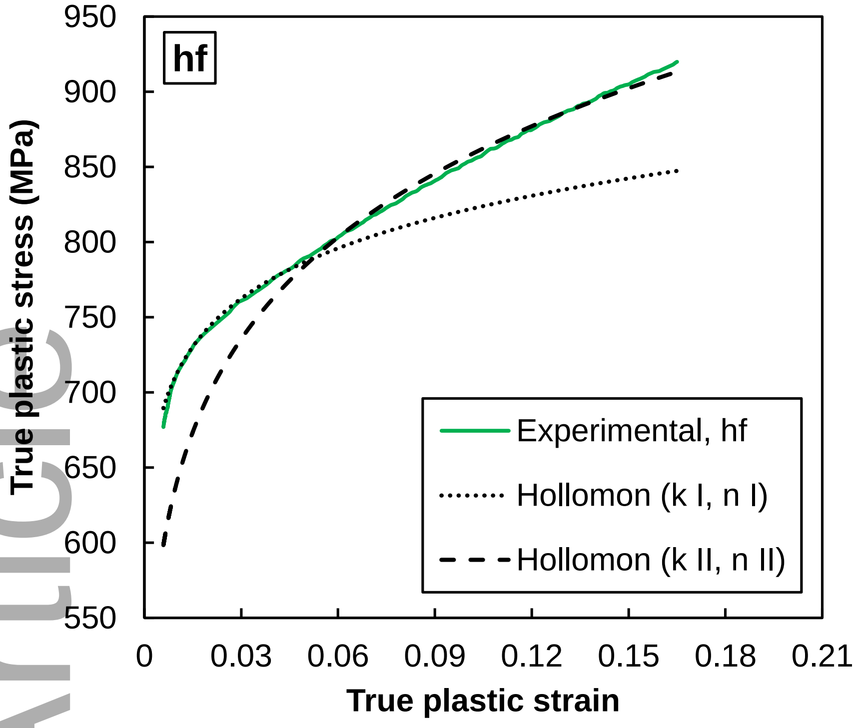

Fig. 15. The true plastic stress-strain curves of LPBF 316L stainless steel specimens with different orientations fitted by Hollomon analysis.

4. Conclusion

The microstructural evolution, tensile properties and strain hardening behavior of as-built LPBF 316L in different orientations were investigated. The results were compared with those obtained for the wrought material as well as with data from the literature. The most important conclusions were drawn as follows:

1. The wrought 316L was composed of equiaxed grains with random orientation and relatively uniform size of about 30 μm and twins, which ensured quasi-isotropic properties. The microstructure of the wrought sample was mainly consisting of HAGBs (~95%) with an average misorientation angle of about 44°. In contrast, the LPBF 316L samples were composed of columnar grains of 100-200 μm size inside the molten pool and fine equiaxed grains of 25-50 μm size in the bottom of the molten pool with a bimodal distribution. The average misorientation angle was about 40° and the fraction of HAGBs was 68-74%. The LPBF 316L had about 25-32% higher values of GNDs.

2. In contrast to conventional 316L, a significant yield strength increase (>200%) and considerable ultimate strength increase (up to 130%) of LPBF material is obtained. These could be explained by the multi-scale microstructural features such as cellular dislocation substructures and bimodal grain size distribution. By considering the contributions of different strengthening mechanisms to the yield strength of the LPBF 316L, the calculated values (549-574 MPa) were in good agreement with the measured range (510-666 MPa). In addition, the strength-elongation balance of the LPBF 316L produced in this study was in the upper range compared to those reported in the literature. It is a good indicator of high energy absorption capabilities of this material.

3. All of the samples showed two-stage strain hardening behavior. The strain hardening exponent of wrought samples was higher than that of the LPBF samples. In addition, this behavior was isotropic in wrought 316L, however it was orientation-dependent in LPBF 316L. The experimental true plastic stress-strain curves were fitted by two-stage Hollomon analysis constants with high accuracy.

CRediT authorship contribution statement

A. T., Y. M. and M. B. performed the conceptualization and methodology; J. M. and S. S. fabricated the specimens and performed tensile tests and optical microscopy measurements; J. S. performed EBSD measurements and Y. M. visualized the EBSD pictures; A. T. and Y. M. wrote the initial version of the manuscript; M. B., B. K. and S. E. reviewed and edited the manuscript. All authors discussed the obtained results.

Data availability

The raw/processed data required to reproduce these findings will be available from the corresponding author upon reasonable request.

Declaration of competing interest

The authors declare that they have no known competing financial interests or personal relationships that could have appeared to influence the work reported in this paper.

References

[1] International Organization for Standardization, Additive Manufacturing. General Principles. Terminology, ISO/ASTM 52900 2021, 2021.

[2] M. Gebler, A.J.M. Schoot Uiterkamp, C. Visser, A global sustainability perspective on 3D printing technologies, Energy Policy 74:158-167, 2014.

[3] J.J. Lewandowski, M. Seifi, Metal additive manufacturing: A review of mechanical properties, Annual Review of Materials Research 46:14.1-14.36, 2016.

[4] Xiaoyu Liang, High cycle fatigue behavior of additive manufactured stainless steel 316L: free surface effect and microstructural heterogeneity, Materials, HESAM Université, 2020, English, NNT: 2020HESAE017, tel-02951486.

[5] C. Kamath, B. El-dasher, G.F. Gallegos, W.E. King, A. Sisto, Density of additively-manufactured, 316L SS parts using laser powder-bed fusion at powers up to 400 W, The International Journal of Advanced Manufacturing Technology 74:65-78, 2014.

[6] I. Tolosa, F. Garciandia, F. Zubiri, F. Zapirain, A. Esnaola, Study of mechanical properties of AISI 316 stainless steel processed by "selective laser melting", following different manufacturing strategies, The International Journal of Advanced Manufacturing Technology 51:639-647, 2010.

[7] B. Zhang, L. Dembinski, C. Coddet, The study of the laser parameters and environment variables effect on mechanical properties of high compact parts elaborated by selective laser melting 316L powder, Material Science & Engineering A 584:21-31, 2013.

[8] C.Y. Yap, C.K. Chua, Z.L. Dong, Z.H. Liu, D.Q. Zhang, L.E. Loh, S.L. Sing, Review of selective laser melting: Materials and applications, Applied Physics Reviews 2(4):041101, 2015.

[9] A. Ahmadi , R. Mirzaeifar, N.S. Moghaddam, A.S. Turabi, H.E. Karaca, M. Elahinia, 2016. Effect of manufacturing parameters on mechanical properties of 316L stainless steel parts fabricated by selective laser melting: A computational framework, Materials & Design 112:328-338, 2016.

[10] J.A. Cherry, H.M. Davies, S. Mehmood, N. P. Lavery, S.G.R. Brown, J. Sienz, Investigation into the effect of process parameters on microstructural and physical properties of 316L stainless steel parts by selective laser melting, The International Journal of Advanced Manufacturing Technology 76:869-879, 2015.

[11] W.M. Tucho, V.H. Lysne, H. Austbo, A. Sjolyst-Kverneland, V. Hansen, Investigation of effects of process parameters on microstructure and hardness of SLM manufactured SS316L, Journal of Alloys and Compounds 740:910-925, 2018.

[12] Z. Zheng, L.F. Wang, B. Yan, Effects of laser power on the microstructure and mechanical properties of 316L stainless steel prepared by selective laser melting, International Journal of Physics B 31(16-19):1744015, 2017.

[13] M.S. Pham, B. Dovgyy, P.A. Hooper, Twinning induced plasticity in austenitic stainless steel 316L made by additive manufacturing, Material Science & Engineering A 704:102-111, 2017.

[14] D. Wang, C.H. Song, Y.Q. Yang, Y.C. Bai, Investigation of crystal growth mechanism during selective laser melting and mechanical property charcterization of 316L stainless steel parts, Materials & Design 100:291-299, 2016.

[15] R. Casati, J. Lemke, M. Vedani, Microstructure and Fracture Behavior of 316L Austenitic Stainless Steel Produced by Selective Laser Melting, Journal of Materials Science & Technology 32, 738-744, 2016.

[16] A. Röttger, K. Geenen, M. Windmann, F. Binner, W. Theisen, Comparison of microstructure and mechanical properties of 316 L austenitic steel processed by selective laser melting with hot-isostatic pressed and cast material, Material Science & Engineering A 678:365-376, 2016.

[17] N.P. Lavery, J. Cherry, S. Mehmood, H. Davies, B. Girling, E. Sackett, S.G.R. Brown, J. Sienz, Effects of hot isostatic pressing on the elastic modulus and tensile properties of 316L parts made by powder bed laser fusion, Material Science & Engineering A 693:186-213, 2017.

[18] M. Shamsujjoha, S.R. Agnew, J.M. Fitz-Gerald, W.R. Moore, T.A. Newman, High Strength and Ductility of Additively Manufactured 316L Stainless Steel Explained, Metallurgical and Materials Transactions A 49A, 3011-3027, 2018.

[19] J. Suryawanshi, K.G. Prashanth, U. Ramamurty, Mechanical behavior of selective laser melted 316L stainless steel, Material Science & Engineering A 696:113-121, 2017.

[20] M. Taheri Andania, M.R. Karamooz-Ravari, R. Mirzaeifar, J. Ni, Micromechanics modeling of metallic alloys 3D printed by selective laser melting, Materials & Design, 137:204-213, 2018.

[21] M. Taheri Andani, M. Ghodrati, M.R. Karamooz-Ravari, R. Mirzaeifar, J. Ni, Damage modeling of metallic alloys made by additive manufacturing, Materials Science & Engineering A 743:656-664, 2019.

[22] A. Biswas, M.R.G. Prasad, N. Vajragupta, H. ul Hassan, F. Brenne, T. Niendorf, A. Hartmaier, Influence of Microstructural Features on the Strain Hardening Behavior of Additively Manufactured Metallic Components, Advanced Engineering Materials 21(7):1900275, 2019.

[23] J.H. Hollomon, Tensile Deformation, Transactions of the Metallurgical Society of AIME 162:268-290, 1945.

[24] P. Ludwik, Elemente der Technologishen Mechanik, Springer, Berlin, 1909.

[25] H.W. Swift, Plastic instability under plane stress, Journal of the Mechanics and Physics of Solids 1(1):1-18, 1952.

[26] B.P. Kashyap, K. Tangri, On the Hall-Petch relationship and substructural evolution in type 316L stainless steel, Acta Metallurgica et Materialia 43(11):3971-3981, 1995.

[27] E. Ulvan, A. Koursaris, The Effect of Grain Size on the Bulk Formability and Tensile Properties of Austenitic Stainless Steel Types 304 and 316, Metallurgical Transactions, 19A:2287-2298, 1988.

[28] M. J. Sohrabi, H. Mirzadeh, and Ch. Dehghanian, Significance of martensite reversion and austenite stability to the mechanical properties and transformation-induced plasticity effect of austenitic stainless steels, Journal of Materials Engineering and Performance 29:3233–3242, 2020.

[29] K. K. Singh, Strain hardening behaviour of 316L austenitic stainless steel, Materials Science and Technology 20:1134-1142, 2004.

[30] F. Khodabakhshi, M.H. Farshidianfar, A.P. Gerlich, M. Nosko, V. Trembošová, A. Khajepour, Microstructure, strain-rate sensitivity, work hardening, and fracture behavior of laser additive manufactured austenitic and martensitic stainless steel structures, Material Science & Engineering A 756:745-561, 2019.

[31] Z. Li, T. Voisin, J.T. McKeown, J. Ye, T. Braun, C. Kamath, W.E. King, Y.M. Wang, Tensile properties, strain rate sensitivity, and activation volume of additively manufactured 316L stainless steels, International Journal of Plasticity 120:395-410, 2019.

[32] S. Afkhami, M. Dabiri, H. Piili, T. Björk, Effects of manufacturing parameters and mechanical post-processing on stainless steel 316L processed by laser powder bed fusion, Materials Science & Engineering A 802 (2021) 140660.

[33] D. Kumar, G. Shankar, K.G. Prashanth, S. Suwas, Texture dependent strain hardening in additively manufactured stainless steel 316L, Materials Science & Engineering A 820 (2021) 141483

[34] T. Papke, M. Merklein, Characterization of Work Hardening Behavior of Additively Manufactured Stainless Steel 316L (1.4404) Using Bulk Metal Forming at Elevated Temperature, Lasers in Manufacturing Conference 2019.

[35] P. Kumar, R. Jayaraj, J. Suryawanshi, U.R. Satwik, J. McKinnell, U. Ramamurty, Fatigue strength of additively manufactured 316L austenitic stainless steel, Acta Materialia 199:225-239, 2020.

[36] Renishaw Bedienungsanleitung: Additive Fertigung von Renishaw: AM250 und AM400 Laserschmelzsysteme, 2016.

[37] Renishaw Data Sheet: SS 316L-0407 powder for additive manufacturing, 2017.

[38] Norm DIN 50125 Dezember 2016. Prüfung metallischer Werkstoffe -Zugproben.

[39] M. Braun, E. Mayer, I. Kryukov, C. Wolf, S. Böhm, A. Taghipour, R.E. Wu, S. Ehlers, S. Sheikhi, Fatigue strength of LPBF and wrought 316L stainless steel: effect of posttreatment and cyclic mean stress, Fatigue & Fracture Engineering Materials & Structures 44(11):3077-3093, 2021.

[40] J. McDavid, Herstellung von AM Proben aus der Legierung 1.4404 durch das SLM-Verfahren und Analyse der Wechselwirkung zwischen Probenorientierung im Druckraum mit den mechanisch-technologischen Eigenschaften [Master thesis], University of Applied Science Hamburg, Institute of Materials Science and Joining Technology, 2019.

[41] M. Braun, S. Hellberg, I. Kryukov, S. Böhm, R.E. Wu, S. Ehlers, S. Sheikhi, Untersuchung der Schwingfestigkeit hybrid additiv und subtraktiv gefertigter Proben aus AISI 316L. 5. Tagung Additiv gefertigte Bauteile und Strukturen. Berlin, Germany, 2020.

[42] M.A. Anam, J.J.S. Dilip, P. Deepankar, B. Stucker, Effect of Scan Pattern on the Microstructural Evolution of Inconel 625 during Selective Laser Melting, Department of Industrial Engineering, University of Louisville, Kentucky, 2014.

[43] J.H. Robinson, I.R.T. Ashton, E. Jones, P. Fox, C. Sutcliffe, The Effect of Hatch Angle Rotation on Parts Manufactured Using Selective Laser Melting, Rapid Prototyping Journal 25(2):289-298, 2017.

[44] Norm DIN EN ISO 6892-1 Februar 2017. Metallische Werkstoffe –Zugversuch.

[45] T. DebRoy, H.L. Wei, J.S. Zuback, T. Mukherjee, J.W. Elmer, J.O.Milewski, A.M. Beese, A. Wilson-Heid,A. De, W. Zhang, Additive manufacturing of metallic components–process, structure and properties, Progress in Materials Science 92:112-224, 2018.

[46] W. Chen, T. Voisin, Y. Zhang, J.B. Florien, C.M. Spadaccini, D.L. McDowell, T. Zhu, Y.M. Wang, Microscale residual stresses in additively manufactured stainless steel, Nature Communications 10(1):1-12, 2019.

[47] Y.M. Wang, T. Voisin, J.T. McKeown, J. Ye, N.P. Calta, Z. Li, Z. Zeng, Y. Zhang, W. Chen, T.T. Roehling, R.T. Ott, M.K. Santala, P.J. Depond, M.J. Matthews, A.V. Hamza, T. Zhu, Additively manufactured hierarchical stainless steels with high strength and ductility, Nature Materials 17:63-71, 2018.

[48] L.F. Liu, Q. Ding, Y. Zhong, J. Zou, J. Wu, Y.L. Chiu, J. Li, Z. Zhang, Q. Yu, Z. Shen, Dislocation network in additive manufactured steel breaks strength-ductility trade-off, Materials Today 21(4):354-361, 2018.

[49] D. Kong, C. Dong, X. Ni, Z. Liang, C. Man, X. Li, Hetero-deformation-induced stress in additively manufactured 316L stainless steel, Materials Research Letters 8(10):390-397, 2020.

[50] Y. Hong, C. Zhou, Y. Zheng, L.Zhang, J. Zheng, X. Chen, B. An, Formation of strain-induced martensite in selective laser melting austenitic stainless steel, Materials Science & Engineering A 740-741:420-426, 2019.

[51] H.D. Carlton, A. Haboub, G.F. Gallegos, D.Y. Parkinson, A.A. MacDowell, Damage evolution and failure mechanisms in additively manufactured stainless steel. Material Science & Engineering A 651:406-414, 2016.

[52] S. Bahl, S. Mishra, K.U. Yazar, I.R. Kola, K. Chatterjee, S. Suwas, Non-equilibrium microstructure, crystallographic texture and morphological texture synergistically result in unusual mechanical properties of 3D printed 316L stainless steel, Additive Manufacturing 28:65-77, 2019.

[53] C. Elangeswaran, A. Cutolo, G.K. Muralidharan, C. de Formanoir, F. Berto, K. Vanmeensel, B.V. Hooreweder, Effect of post-treatments on the fatigue behaviour of 316L stainless steel manufactured by laser powder bed fusion, International Journal of Fatigue 123:31-39, 2019.

[54] Y. Zhong, L. Liu, S. Wikman, D. Cui, Z. Shen, Intragranular cellular segregation network structure strengthening 316L stainless steel prepared by selective laser melting, Journal of Nuclear Materials 470:170-178, 2016.

[55] Y.J. Yin, J.Q. Sun, J. Guo, X.F. Kan, D.C. Yang, Mechanism of high yield strength and yield ratio of 316 L stainless steel by additive manufacturing, Materials Science & Engineering A 744:773-777, 2019.

[56] Z. Sun, X. Tan, S.B. Tor, C.K. Chua, Simultaneously enhanced strength and ductility for 3D-printed stainless steel 316L by selective laser melting, NPG Asia Materials 10: 127-136, 2018.

[57] H. Qu, J. Li, F. Zhang, J. Bai, Anisotropic cellular structure and texture microstructure of 316L stainless steel fabricated by selective laser melting via rotation scanning strategy, Materials & Design 215:110454, 2022.

[58] I. P. Bajaj, A. Hariharan, A. Kini, P. Kürnsteiner, D. Raabe, E.A. Jagle, Steels in additive manufacturing: A review of their microstructure and properties, Materials Science & Engineering A 772:138633, 2020.

[59] A. B. Spierings, T.L. Starr, K. Wegener, Fatigue performance of additive manufactured metallic parts, Rapid Prototyping Journal 19(2):88-94, 2013.

[60] A. Riemer, S. Leuders, M. Töhne, H.A. Richard, T. Tröster, T. Niendorf, On the fatigue crack growth behavior in 316L stainless steel manufactured by selective laser melting, Engineering Fracture Mechanics. 120:15-25, 2014.

[61] P. A. Kuznetsov, A.A.Zisman, S.N. Petrov, I.S. Goncharov, Structure and mechanical properties of austenitic 316L steel produced by selective laser melting, Russian Metallurgy 10:930-934, 2016.

[62] S. Pillot, Fusion laser sélective de lit de poudres métalliques, Techniques de l'ingénieur BM7900, 2016.

[63] E. Liverani, S. Toschi, L. Ceschini, A. Fortunato, Effect of selective laser melting (SLM) process parameters on microstructure and mechanical properties of 316L austenitic stainless steel, Journal of Materials Processing Technology 249:255-263, 2017.

[64] A.B. Kale, J. Singh, B.K. Kim, D.I. Kim, S.H. Choi, Effect of initial microstructure on the deformation heterogeneities of 316L stainless steels fabricated by selective laser melting

processing, Journal of Materials Research and Technology 9(4):8867-8883, 2020.

[65] A. Röttger, J. Boes, W. Theisen, M. Thiele, C. Esen, A. Edelmann, R. Hellmann, Microstructure and mechanical properties of 316L austenitic stainless steel processed by different SLM devices, The International Journal of Advanced Manufacturing Technology 108:769-783, 2020.

[66] M. Janecek, K. Tangri, Substructure evolution and flow behaviour of AISI 316L stainless steel polycrystals at room temperature, Material Science & Engineering A 138(2):237-245, 1991.

[67] Y. Wei, Y. Li, L. Zhu, Y. Liu, X. Lei, G. Wang, Y. Wu, Z. Mi, J. Liu, H. Wang, H. Gao, Evading the strength- ductility trade-off dilemma in steel through gradient hierarchical nanotwins, Nature Communications 5:3580, 2014.

Research highlights

- Bimodal distribution and orientation dependency of grains in LPBF 316L SS
- Higher fraction of LAGBs and GNDs in LPBF 316L and substantial strengthening
- Significant increase (~ 130%) in strength without remarkable reduction in elongation
- Comparable strength-elongation balance (~ 26122 MPa%) with the literature
- Two-stage, lower exponents, and orientation dependency of LPBF 316L strain hardening

The strengthening mechanisms and strain hardening of 316L stainless steel fabricated by different strategies of laser-based powder bed fusion (LPBF) was comprehensively investigated. A high strength-elongation balance (up to 26122 MPa%) was obtained for the LPBF tensile specimens and the contributions of different strengthening mechanisms were calculated. The plastic region of true stress-strain curves is successfully predicted with two-stage Hollomon analysis results.

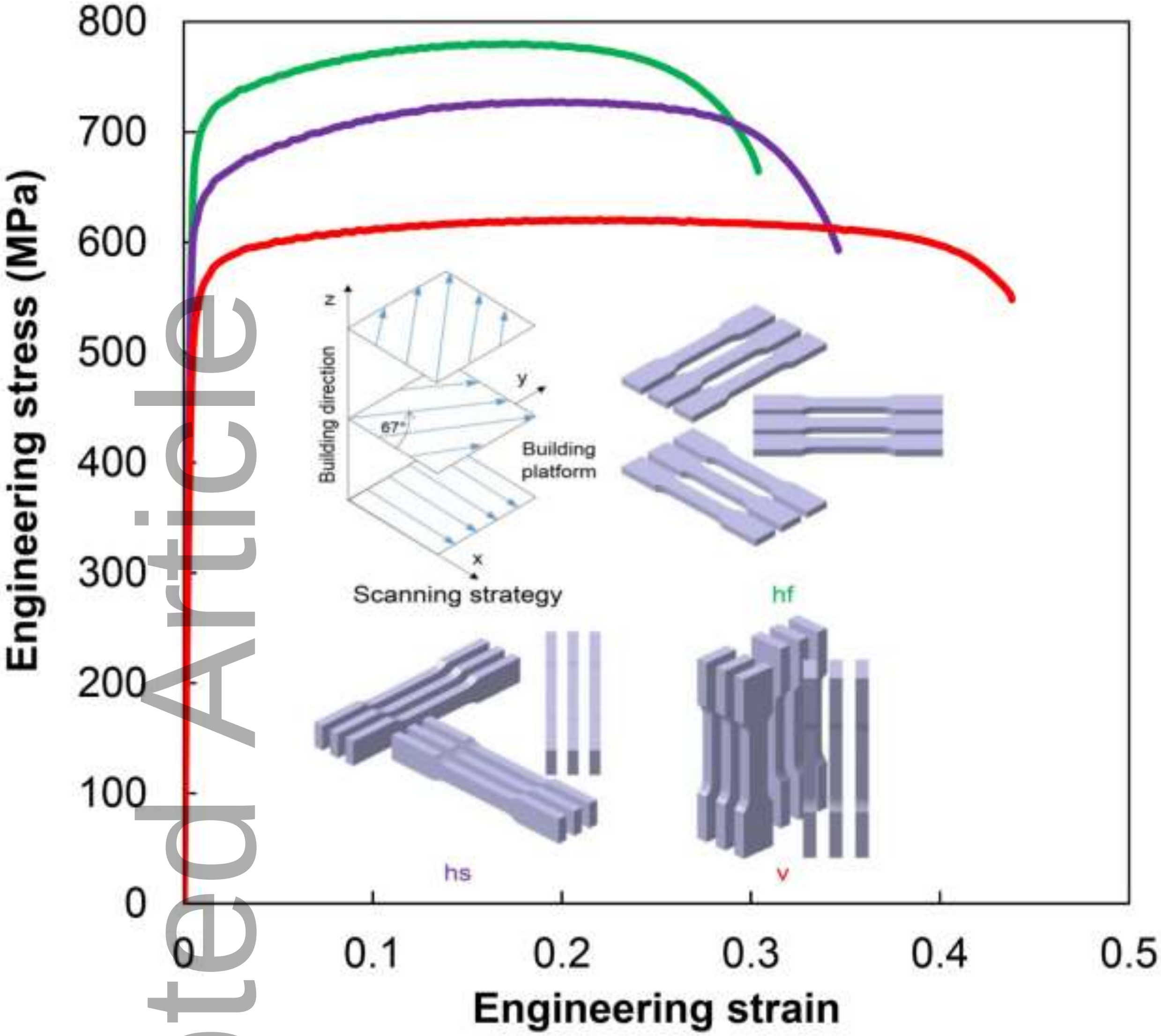

Engineering stress (MPa)
800
700
600
500
400
300
200
100
0
0
0.1
0.2
0.3
0.4
0.5
Engineering strain
Building direction
z
y
x
67°
Building platform
Scanning strategy
hf
hs
v